Flow and Heat Transfer of Single- and Two-Phase Boiling of Nanofluids in Microchannels

Flow and heat transfer of single and two-phase boiling of nanofluids in microchannels

Gail Duursma[1*], Khellil Sefiane[1], Alexandre Dehaene[2], Souad Harmand[2], Yuan Wang[3]

[1]School of Engineering, The University of Edinburgh, King's Buildings, Mayfield Road, Edinburgh EH9 3JL, United Kingdom

[2]ENSIAME, Université de Valenciennes, France

[3]Science and Technology on Scramjet Laboratory, National University of Defense Technology, Hunan, Changsha 410073, People's Republic of China

[*]Address correspondence to Dr Gail Duursma, School of Engineering, The University of Edinburgh, The King's Buildings, Mayfield Road, Edinburgh EH9 3JL, UK

E-mail: gail.duursma@ed.ac.uk

Phone Number: 0 (+44) 131 650 4868, Fax Number: 0 (+44) 131 650 6551

ABSTRACT

Experiments using nanofluids in horizontal, rectangular high-aspect-ratio microchannels were performed where heat was provided electrically to the microchannel wall to bring about heating and phase change whilst recording temperature (via infrared camera) and channel pressure drop. High-speed video captured images of boiling two-phase flow through the transparent microchannel wall. Nanofluids used were solutions of aluminium oxide in ethanol with particle concentrations from 0.01% to 0.1%, with pure ethanol as reference. Fluid mass flux ranged from Reynolds numbers of 2.3 to 18.1 and heat fluxes from 1.5 to 9 kWm^{-2}. Friction factors for the nanofluids were evaluated. Single phase fluid pressure drop did not vary significantly with nanoparticle concentration. When flow boiling occurred, the two-phase flow pressure drop was unstable and fluctuating. Inlet pressures had greater amplitude of oscillation but similar frequency to outlet pressures. Heat transfer increased with the presence of nanoparticles compared with pure ethanol. Moreover evaporation from the meniscus was studied. There is a sudden evaporation phenomenon where the meniscus rapidly forms. Infrared data demonstrate the effect of heat flux on temperature distribution near the three phase contact line. Nanoparticles enhance boiling heat transfer coefficients, peaking at a concentration of 0.05% with significant enhancement over pure ethanol.

INTRODUCTION

The need for more effective heat transfer technologies for high-thermal density devices is becoming paramount as the operational speed and power of such devices is becoming limited by the cooling rate. Such technologies include microscale flows in microchannels [1]-[6]. In addition to conventional heat transfer enhancement methods, novel ideas for improving heat transfer capacity by using advanced fluids with greater potential to provide better thermal characteristics offer new opportunities to improve cooling performances. Bogojevic *et al.* [5,6] and Barber *et al.* [2,3,4] have reported works on flow boiling heat transfer in microchannels and its potential for cooling micro-systems.

Liquids laden with nanometre-sized solid particles exhibit excellent stability and do not experience large scale sedimentation thanks to the size effect and Brownian motion of nanoparticles. Nanofluids as a colloidal mixture of nanoparticles (1-100 nm) and a base liquid, have been identified as a new type of fluids with enhanced thermal properties, Choi and Eastman [7]. Various types of nanoparticles have been reported in literature including metallic particles (*e.g.* Cu, Al, Fe, Au, and Ag) and non-metallic (oxides) particles (*e.g.* Al_2O_3, CuO, Fe_3O_4, TiO_2, SiC and ZrO_2) [8-26]. Some commonly used base liquids for suspending such nanoparticles are water, oil, acetone, decene and ethylene glycol. There are also some recent studies on refrigerant-based nanofluids, (Trisaksri and Wongwises [23], Park and Jung [24, 25]. In flow configuration, the presence of nanoparticles may influence the pressure drop characteristics of single phase and flow boiling within small-scale channels and consequently affect the overall performances of cooling systems. Several studies have been undertaken, to investigate specific aspects of the flow of nanofluids, among these aspects; the laminar entrance flow region and fully developed flow region (Hwang *et al.* [18],

Rea *et al.* [19]), transition flow (Sharma *et al*. [27], Dong and Leyuan [28]) as well as turbulent flow (Xuan and Li [29], Williams *et al*. [21], Sharma *et al*. [27], Duangthongsuk and Wongwises [20], Fotukian and Nasr Esfahany [30])). Dong and Leyaun [28] studied single phase forced convection of Al_2O_3-water nanofluids in circular minichannels (d_{in} = 1.09 mm) and reported an increase of friction factor with increasing nanoparticle concentration. However, the nanoparticle effect diminished significantly at higher Reynolds number. They described a prolonged hydrodynamic developing length and an early transition from laminar to turbulent flow using nanofluids. A pressure drop penalty was also reported by Fotukian and Nasr Esfahany [30] using CuO-water nanofluids in an annular tube with d_{in} = 5 mm and d_{out} = 32 mm. In contrast, some works showed minimal rise in pressure drop using nanofluids (Li and Xuan [31], Rea *et al.* [19], and Duangthongsuk and Wongwises [20]), especially for dilute nanofluids. It was argued that nanofluids can be treated as homogeneous fluids and the conventional friction factor correlations can be extended to nanofluids. It is worth noting that the aforementioned studies were mostly carried out in large scale or mini-scale circular tubes. Nanofluid convective flows in micro-scale channels with different cross-sectional geometries still needs further investigation. Beside single phase pressure drop studies, two-phase boiling has received recent attention from researchers. Despite this, knowledge of nanofluid flow boiling heat transfer in micro-scale is still quite limited and the majority of studies on the subject were conducted in pool boiling. Das *et al.* [32] investigated pool boiling heat transfer of Al_2O_3-water nanofluids. They found that added nanoparticles have pronounced influence on deteriorating boiling heat transfer. On the contrary, Wen and Ding [33] concluded that alumina based nanofluids can significantly enhance boiling heat transfer. The enhancement increased with increasing particle concentration and a 40% heat transfer coefficient enhancement was reported at a particle loading of 1.25% by weight. Moreover, an impressive ~200% heat transfer coefficient enhancement was achieved by White [34] using

ZnO-water nanofluid on a ZnO coated stainless steel surface. In this study, the achieved heat transfer enhancement was correlated to increased nucleation sites density due to surface coating. Similar trends were also obtained by Z. Heris [35]. The author [35] studied CuO/ethylene glycol-water nanofluids used for pool boiling experiments. It was concluded that heat transfer coefficient was significantly enhanced by nanofluids, and the heat transfer enhancement increased with increasing particle concentration. A 55% heat transfer coefficient enhancement was reached at 0.5% particle loading by weight. The authors highlighted the importance of the interactions between nanofluids and the boiling surface. Kole and Dey [36] conducted experimental investigations on heat transfer characteristics of ZnO-ethylene glycol nanofluids during pool boiling. Similar to Zeinali Heris [35], the boiling heat transfer coefficient was found first to increase and then drop as the nanoparticle concentration increases from 0 to 2.6vol%. The peak in heat transfer coefficient occurred at 1.6 vol% and an increase of 22% was reported. The decrease in boiling heat transfer was considered to be the consequences of the reduced ZnO concentration for heat transfer and the blockage of active nucleation sites, both of which were caused by deposition of nanoparticles. The existence of an optimum nanoparticle concentration for heat transfer enhancement was later established in many studies [2], [35]-[40]. Chang *et al.* [37] investigated the effects of particle volume fraction on spray heat transfer performance using Al_2O_3-water nanofluids. The fractions of the tested nanofluids ranged from 0 to 0.05 vol%. The optimal heat transfer performance was achieved at 0.001vol%, whereafter heat transfer deteriorated with further increases of volume fraction. Based on the SEM images and surface composition analysis, it was concluded that the higher the fraction, the thicker the nanoparticle deposition layer formed on the heated surface, which hinders convective heat transfer. Jung *et al.* [40] found that boiling heat transfer coefficient would become lower than that of the base liquid as the concentration of nanoparticles increases. Apart from the blocking of the active nucleation

sites, they explained that the increase of conduction resistance by nanoparticle deposition also contributed to heat transfer deterioration. However, Huminic and Huminic [41] described the positive impact of nanoparticles on the thermal performance of a two-phase closed thermosyphon. They also found that the thermal resistance decreases as the nanoparticle volume concentration increases. Recently, Wen [42] concluded that both particle deposition effect, and the collective effect of particles suspended in liquid, could affect the boiling heat transfer significantly. The relative size between particles and surface geometry was found quite influential. There are few studies published on flow boiling heat transfer with nanofluids in microchannels. The most widely reported conclusions were the increase of critical heat flux (CHF). Vafaei and Wen [43] discussed the effect of nanoparticles on critical heat flux during subcooled flow boiling of aqueous based alumina nanofluids in a 510 μm single microchannel. Compared with pure de-ionized water, an increase of ~ 51% in the critical heat flux was achieved under very low nanoparticle concentrations (~0.1 vol%). Furthermore, detailed observations of the boiling surface showed that as particles concentration increased, fouling effects were more noticeable at the channel outlet, resulting in altered surface conditions. Thus nanoparticle deposition and the consequent surface modification were argued to be responsible for CHF enhancement. Kim *et al.* [44] evaluated the CHF enhancement using water-based Al_2O_3 nanofluids. Similarly, the CHF of Al_2O_3 nanofluids was enhanced by up to ~ 70% in flow boiling compared to de-ionized water. As a result of the deposition of Al_2O_3 nanoparticles on the tube inner surface, the CHF enhancement contributed to the enhanced wettability of the liquid film onto the heater surface. Interestingly, no significant change of CHF was observed when Al_2O_3 nanoparticle concentration increased from 0.001 vol% to 0.1 vol%. Furthermore, the flow boiling heat transfer coefficient of nanofluids is also found to be largely dependent on the stability of the nanofluid. Henderson *et al.* [45] studied flow boiling heat transfer of R-134a-based

nanofluids in a horizontal tube. The R134a-based SiO_2 nanofluid stability was relatively poor, where a 55% heat transfer decrease was encountered. However, excellent dispersion was achieved for a mixture of R-134a and polyolester oil with CuO nanoparticles, and more than 100% heat transfer coefficient enhancement was found compared with the base liquid. Similarly, Park *et al.* [46] also reported decreased heat transfer in unstable R-134a-based nanofluids. They suggested that the modification of particle surface properties could improve the nanofluid flow boiling heat transfer performance.

Although nanofluids were reported to have improved thermal performance of liquids compared to pure liquids while inducing very little rise in pressure drop ([45], [47]), the application of nanofluids is still in its infancy. Many questions regarding heat transfer characteristics and the underlying mechanisms still to be elucidated.

EXPERIMENTAL APPARATUS AND PROCEDURE

General description

The experimental apparatus and configuration (see Figure 1) consists of a micro-channel coated with a layer of tantalum on its outer surface. Both ends of this layer were connected to a DC power supply to ensure the micro- channel heating. This transparent heating technique was employed to guarantee the flow visualisation using a CCD camera as well as an infrared camera for thermal mapping, see Barber *et al.* [2-4]. K-type thermocouples were located at the inlet and outlet of the channel to measure the corresponding temperatures. A high speed camera (NanoSense® MKIII) was installed above the test section to provide synchronised observations. The rate of this camera was set from 500 fps to 2500 fps depending on the different visualization requirements.

The mass flow rate was controlled using a syringe pump. All the tests were conducted at atmospheric pressure in a range of channel sizes. The horizontal, rectangular high-aspect-ratio microchannel dimensions were: W_{in}=8 mm, d_{in}=0.8 mm and d_{wall}=0.54 mm. The test fluid is pure ethanol with nanoparticles. The nanoparticles are provided by SigmaAldrich®. In this particular study, we used aluminium oxide particles, Al_2O_3, in ethanol. The mass of nanoparticles was measured using a micro-balance and solutions were prepared with the following concentration; 0.01%, 0.05% of 0.1% (in ethanol). The mixture was then put in an ultrasonic bath for at least two hours and a half before performing the experiments. The experimental uncertainties mainly came from pump velocity (± 0.5 %), input power (voltage: ± 0.2 % and current: ± 0.5 %), channel dimension (depth and thickness: ± 10 %, width and length: ± 2 %), temperature measurements (IR camera: ± 1 %, thermocouples: ± 0.05 K).

Nanoparticles (Sigma Aldrich®) were purchased in powder form. The particle size was less than 50 nm according to the manufactures specifications. The nanofluid concentration was described in volume percentage, noted as vol%. Nanofluids were prepared by measuring the required mass of nanoparticles using a microbalance and dispersing the nanoparticles into the known volume of base liquid (ethanol).

A magnetic stirrer was used for nanofluids dispersion. Nanofluid solutions which were made by magnetic stirrer and ultrasonic bath were compared. Ultrasonication ensured better suspension stability. Therefore, an ultrasonic bath was used for nanofluids preparation. Most importantly, nanofluids made by ultrasonic bath could stay well-suspended for at least 7 hours, which was stable long enough for each set of experiment, as shown in Figure 2. The physical properties of nanofluids such as density and dynamic viscosity which are needed for the related data reduction were measured in the laboratory.

During single phase flow, the inlet and outlet pressures of the micro-channel test section were measured via a pair of pressure transducers located at the channel entrance and exit. The pressure readings were taken with a National Instrument® Data Acquisition card at a frequency of 200 Hz. The offset pressures resulted from the background noises were recorded prior to each test when the channel was filled with stagnant working fluid. Then the offset pressures were subtracted from the acquired raw data. Darcy friction factor was calculated and compared with the predictions of conventional theory for both pure and nanofluids.

After each test with nanofluids, all the components in the entire flow loop including connecting pipes, valves, reservoir and micro-channel test section were thoroughly cleaned by running water, ultrasonic bath and dried by compressed air.

In addition to the above, Infra-red thermography is used to map the wall temperature of channels. ThermoVision® 900 infrared camera was used to record the temperature profiles across the micro-channel outer surface. It has a resolution of 204 pixel × 88 pixels and an accuracy of ±1 K or ±1% for different temperature ranges. The highest frequency was 50 fps and was adopted in all experiments. The ThermaCAM Researcher Professional® software was used to analyse the IR image sequences and extract temperature profiles.

RESULTS AND ANALYSIS

Analysis of pressure drop and friction factor deduction

A series of single phase pressure drop measurements were performed with an increasing volume flow rate from 1 $ml \cdot min^{-1}$ to 144 $ml \cdot min^{-1}$ (the limit of the used pump). Experiments for each flow rate in each micro-channel were repeated for three times on different days. It was found that measured pressure drop variations were less than 5%, indicating good reproducibility. These three measurements in each test series were averaged and used for friction factor calculation. The difference between inlet and outlet pressures gave the total

pressure drop ΔP_{Total}. The micro-channel and the connection pipes are schematically illustrated in Figure 3.

The direct pressure drop ΔP_{Total} includes frictional pressure drop in the micro-channel and Pipe 1 – Pipe 4 as well as the minor pressure drop due to abrupt expansion or contraction at pipe connections and that in hydrodynamically developing flow. The total pressure drop comprised the following four components (where subscript fn refers to friction, sn to abrupt area change, cd to microchannel hydrodynamic development and cf to microchannel fully developed flow):

$$\Delta P_{\text{Total}} = \sum_{\text{n=1,2,3,4}} \Delta P_{\text{fn}} + \sum_{\text{n=1,2,3,4}} \Delta P_{\text{sn}} + \Delta P_{\text{cd}} + \Delta P_{\text{cf}} \quad (1)$$

where $\sum_{\text{n=1,2,3,4}} \Delta P_{\text{fn}}$ is the sum of frictional pressure drop in the four connection pipes (White [48]):

$$\Delta P_{\text{fn}} = f \frac{L_{\text{n}}}{d_{\text{in,n}}} \cdot \frac{\rho u_{\text{pipe}}^{2}}{2}, \quad \text{n} = 1,2,3,4 \quad (2)$$

where L_{n} and d_{in} are the length and inner diameter of the pipes, ρ is the liquid density, u_{pipe} is the liquid velocity and f is the Darcy friction factor in circular tube; here $f = 64/Re$.

$\sum_{\text{n=1,2,3,4}} \Delta P_{\text{sn}}$ is the pressure drop due to abrupt expansion and contraction at pipe connections, (illustrated as locations 1, 2, 3 and 4 in Figure 3) and is estimated as:

$$\Delta P_{\text{sn}} = K_{\text{n}} \frac{\rho u_{\text{n}}^{2}}{2}, \text{n} = 1,2,3,4 \quad (3)$$

where u_{n} is the velocity head at each location and K_{n} are the loss coefficients. The pipes and the micro-channel test section are connected with a large cone angle, *i.e.* $2\theta \approx 180°$ and therefore can be considered as an abrupt expansion and contraction. The expansion loss

coefficients for the abrupt expansion from a small pipe with a diameter d to a large pipe with a diameter D are therefore (White [48]) calculated from: note that K_n is based on the velocity head in the small pipe.

$$K_n = \left(1 - \frac{d^2}{D^2}\right)^2, n = 1 \text{ and } 3 \quad (4)$$

Thus K_1 = 0.79 and K_3 = 0.991, 0.986 and 0.948 for the 571 μm, 762 μm and 1454 μm channel respectively.

The contraction loss coefficient for positions 2 and 4:

$$K_n \approx 0.42\left(1 - \frac{d^2}{D^2}\right), n = 2 \text{ and } 4 \quad (5)$$

yields K_4 = 0.37 and K_2 = 0.418, 0.417 and 0.409 for the channels with d_h = 571 μm, 762 μm and 1454 μm respectively.

Pressure drop in the hydrodynamic developing region in the micro-channel, ΔP_{cd}, and is calculated from correlation (6) (Shah and London [49]):

$$\Delta P_{cd} = \frac{1}{2}\rho u^2\left(13.74\sqrt{L_{df}^+} + \frac{1.25 + 64L_{df}^+ - 13.74\sqrt{L_{df}^+}}{1 + 0.0002\,1(L_{df}^+)^{-2}}\right) \quad (6)$$

where L_{df}^+ is dimensionless hydrodynamic developing flow entrance length based on the hydrodynamic developing entrance length L_{df}:

$$L_{df}^+ = \frac{L_{df}/d_{in}}{Re} \quad (7)$$

where d_{in} is the inner diameter, here taken as the hydraulic diameter of the rectangular channel.

According to Shah and London [50], the values of L_{df}^+ can be computed as:

$$L_{\mathrm{df}}^{+} = 0.0565 \text{ for } Re > 400;$$
$$L_{\mathrm{df}}^{+} = 0.0565 + \frac{0.60}{Re(1+0.035Re)} \text{ for } Re < 400 \tag{8}$$

Thus, $\Delta P_{\mathrm{cf}} = \Delta P_{\mathrm{Total}} - \sum_{\mathrm{n=1,2,3,4}} \Delta P_{\mathrm{fn}} - \sum_{\mathrm{n=1,2,3,4}} \Delta P_{\mathrm{sn}} - \Delta P_{\mathrm{cd}}$ is the frictional pressure drop within the channel in the fully developed flow region. For the highest flowrates in the 1454 μm micro-channel, the hydrodynamic entrance length is longer than the channel length, thus ΔP_{cf} is the frictional pressure drop in developing flow conditions after subtracting $\sum_{\mathrm{n=1,2,3,4}} \Delta P_{\mathrm{fn}}$ and $\sum_{\mathrm{n=1,2,3,4}} \Delta P_{\mathrm{sn}}$ .The Darcy friction factor is then calculated as:

$$f = \frac{2\Delta P_{\mathrm{cf}} d_{\mathrm{h}}}{\rho u^2 L} \tag{9}$$

where d_{h} is the micro-channel hydraulic diameter, ρ is the liquid density, u is the mean liquid velocity in the micro-channel and L is the channel length.

According to the calculation, the minor pressure drops increase with increasing Reynolds number, and the relevant importance of $\sum_{\mathrm{n=1,2,3,4}} \Delta P_{\mathrm{fn}}$, $\sum_{\mathrm{n=1,2,3,4}} \Delta P_{\mathrm{sn}}$ and ΔP_{cd} changes in the ranges of 0.16 % – 0.25 %, 0.01 % – 0.35 %, and 0.81 % – 32.1 % respectively, thus the frictional pressure drop is 67.4 % to 98.9 % of the measured total pressure drop. The uncertainty of the friction factor is estimated to be 19 %.

Two properties of nanoparticle suspensions involved in calculating the friction factor are density and dynamic viscosity of the nanofluids, which are different from the original base liquid because of the additional particles. For the nanoparticle suspension, the effective density is estimated following Xuan and Roetzel [8]:

$$\rho_{\mathrm{nf}} = \phi\rho_{\mathrm{p}} + (1-\phi)\rho_{\mathrm{f}} \tag{10}$$

where ϕ is the volume fraction of nanoparticles, ρ_p and ρ_f are the densities of the nanoparticle material and the base liquid respectively.

Few theoretical formulas are available to calculate the nanofluid viscosity. In the present study, the extended Einstein's equation by Brinkman [51] is used to estimate the effective viscosity of nanofluids with moderate particle concentration:

$$\mu_{nf} = \mu_f \frac{1}{(1-\phi)^{2.5}} \tag{11}$$

where μ_{nf} is the effective viscosity of the nanofluid with a particle volume fraction of ϕ, and μ_f is the pure liquid viscosity.

Single phase friction factor of nanofluids

In order to investigate the friction factor of nanofluids and the validity of conventional friction factor correlations, pressure drops of pure ethanol were used as a reference to compare with those of the ethanol-based Al_2O_3 nanofluids. Four different particle volume fractions were tested to reveal the influence of particle concentration on single phase friction factor in high aspect ratio micro-channels.

Figure 4 (a) to (c) show the friction factor versus Reynolds number in the three channels respectively. Nanoparticle volume fractions are 0 (*i.e.* pure ethanol), 0.01 vol%, 0.05 vol%, 0.1 vol% and 0.5 vol%. The influence of nanoparticles on single phase friction factor is found to be insignificant under the test conditions in the present study. This indicates that the tested nanofluids can be considered as dilute suspensions. Some differences can be found in different channels. In the 571 μm channel, as shown in Figure 4 (a), results of all the five concentrations nearly overlap and are all predicted by the conventional theory within ±30%. Better agreement with the predictions can be found at lower Reynolds number region, but the

friction factor slightly drops below the prediction when *Re* is higher. The impact of nanoparticle concentration is slightly more detectable in low Reynolds number region. In the 762 μm channel (Figure 4 (b)), nanoparticles effect vanishes at higher Reynolds number range. The difference among the friction factors of different-concentrated nanofluids is more obvious in the low Reynolds number region. However, the effect of concentration is not conclusive. It can also be noticed that as *Re* increases, the friction factors of nanofluids gradually become lower than the pure ethanol results.

The friction using nanofluids in the 1454 μm channel show the poorest agreement with the conventional theory predictions. Most of the data fall outside the $\pm 30\%$ range. Moreover, the effect of nanoparticle concentration is more detectable in low *Re* region. At $Re = 2.82$, the friction factor increases as particle volume fraction increases from 0.01 vol% to 0.5 vol%.

The insignificant effect of nanoparticle concentration on single phase friction factor was previously reported by Li and Xuan [31], Rea *et al.* [19] Duangthongsuk and Wongwises [20], and with conventional or mini-scale circular tubes, especially for dilute nanofluids. This implies that nanofluids can be treated as homogeneous fluids and the conventional friction factor correlations can be extended to nanofluids.

According to Figure 4, the data sets just overlap at higher Reynolds numbers; the friction factors of nanofluids become slightly lower than the friction factor of pure ethanol. In addition to possible influences from particle deposition and changes of surface condition, the nanoparticles also affect the viscosity of the suspension. Viscosity is increased with increasing particle concentration according to the existing correlations in Xuan and Roetzel [8]. However, the particle concentrations in the present study were relatively low, thus only minor changes of viscosity are found, and consequent variations of single phase friction factor are slight. Single phase flow was achieved at lower heat fluxes. Further increase of

imposed heat flux led to boiling ensuing within the microchannel. This will be examined in the following section.

Two-phase boiling heat transfer

Increasing the applied power, leads to a transition to a two-phase boiling regime. This regime is studied by measuring pressure drops and wall temperature profile. Pressure drops across the microchannel were obtained and their oscillations investigated. In Figure 5 the inlet and outlet pressure signals are presented. A comparison between single phase and two-phase pressure measurements are highlighted. Periodic oscillations are clearly identifiable in the case of two-phase flow. Detailed pressure drop is given in Figure 6; inlet pressures have higher amplitudes than those at the outlet. There are rapid (short timescale) oscillations and slow (long timescale) oscillations superimposed, as can be seen in the magnified results for one second in Figure 6b.

In addition to pressure oscillations measurements, wall temperature was recorded simultaneously. Figure 7 shows an example of a map of wall temperature acquired by the infrared camera. Temperature varies across the surface area and increases in the flow direction. The spatial temperatures and flux are used to estimate local heat transfer coefficients along the channel axial direction:

$$h_{\text{local}} = \frac{q}{T_{\text{W,local}} - T_{\text{L,local}}} \tag{12}$$

where $T_{\text{W,local}}$ is the local temperature of the channel outer surface measured using the IR camera, $T_{\text{L,local}}$ is the local liquid temperature. This local liquid temperature was calculated based on the assumption that all the effective applied heat flux was used to heat up the liquid. This leads to the following energy balance,

$$2z(W_{\text{in}} + d_{\text{in}}) \cdot q = c_p G A_{\text{c}} (T_{\text{L,z}} - T_{\text{in}}) \tag{13}$$

where A_c is the channel cross-sectional area, c_p is the specific heat capacity, G is the mass flux and q the heat flux. So the liquid temperature can be written as

$$T_{\text{L,z}} = \frac{2q(W_{\text{in}} + d_{\text{in}})}{c_p G A_{\text{c}}} \cdot z + T_{\text{in}} \qquad \text{for} \qquad z<z_{\text{sat}} \tag{14}$$

where $T_{\text{L,z}}$ (or $T_{\text{L,local}}$) is the local liquid temperature at a distance z (mm) from the channel inlet. Once the saturation temperature is reached, the liquid temperature remains at saturation

$$T_{\text{L,z}} = T_{sat} \text{ for } z>z_{\text{sat}} \tag{15}$$

where

$$z_{sat} = \frac{\dot{m} c_p (T_{sat} - T_{in})}{2q(W_{in} + d_{in})} \tag{16}$$

The heat transfer coefficient was extracted from the infrared temperature data using eq. (12). Using the stated measurement uncertainties, the error estimate in heat transfer coefficient was found to be of the order ± 6 %.

This is a local heat transfer coefficient varying with length along the channel as the temperature is a function of the distance downstream. Heat transfer coefficients for a range of nanofluid concentrations are given in Figure 8 for two different heat fluxes and indicate heat transfer coefficient as a function of position in the microchannel. The difference between the upstream and downstream positions' heat transfer coefficients are more pronounced for higher applied power. Furthermore heat transfer coefficients increase with increasing nanoparticle concentration and exhibit a maximum at a concentration of 0.05%. The heat transfer coefficient is then plotted as a function of nanoparticle concentration at three different positions, *i.e.* upstream, middle and downstream. This is presented in Figure 9 for

three different mass fluxes (Reynolds numbers). It can be seen that the maximum heat transfer coefficient occurs at a nanofluid concentration of 0.05% for a range of Reynolds numbers for all positions along the channel. It is clear, from Figure 9 that there is a heat transfer enhancement brought about by nanoparticles at concentration below 0.05%. This seems consistent for all Reynolds numbers and any position along the channel. Heat transfer enhancement is however greatest at positions further downstream. The heat transfer coefficient is enhanced by a factor of up to five-fold when comparing pure liquid to a nanofluid at 0.05% concentration. At higher nanoparticle concentration the enhancement to heat transfer is reduced relative to that at 0.05%.

Visualisation of the two-phase nature of the flow was possible with the equipment and provides details of vapour bubble growth in a microchannel as shown in Figure 10.

Flow patterns for nanofluids boiling in the microchannel were characterised using high speed imaging. These seem to be consistent with flow patterns known and observed during these experiments, as given in Figure 11, for pure liquids. The presence of nanoparticles appeared to make the meniscus more stable than that for pure ethanol alone, especially at higher flowrates and higher applied power. The experimental observations of flow patterns highlighted the importance of heat transfer near the contact line. This will be investigated and presented in the following section.

Heat and Mass Transfer near the contact line

It was concluded from the previous section that heat and mass transfer near the three phase contact line is crucial. In what follows we present experimental data investigating the behaviour of a stationary meniscus undergoing heat and mas transfer. A meniscus was maintained in a vertical micro-channel to study the evaporation process and elucidate underlying heat transfer mechanism near the contact line. A controllable heat flux was

applied on the channel outer surface, and the syringe pump flow rate was adjusted to keep the meniscus at a constant position within the channel, therefore the flow rate could be considered as the evaporation rate at the meniscus. The evaporation rate as a function of heat flux was obtained.

Simultaneously, the transient temperature profiles of the channel outer surface at and around the contact line region were acquired by the infrared (IR) camera which was operated at 50 fps and the ThermaCAM Researcher Professional® software was used to analyse the IR image sequences. The synchronous visualisation was provided by the high speed camera. The forces acting on the meniscus are shown schematically in Figure 12. The liquid is adsorbed onto the wall by strong intermolecular forces. The meniscus shape is determined by the relative magnitude of surface tension, adhesion and gravity forces. Capillarity is more significant in the smaller microchannel due to the small mass of liquid used. With no applied heat flux to the micro-channel, the meniscus was found to recede in the channel upon evaporation. Once heat flux was applied, the interface started to move upwards due to liquid surface tension, which decreases with increasing temperature. Further increase of heat flux achieved a stationary meniscus. The meniscus was considered stable when it maintains a stationary position in the channel without any deformation. A stable meniscus was maintained with the help of a syringe pump, the pumping speed of which equalled the liquid evaporation rate. Figure 13 shows the evolution of the meniscus in a channel with hydraulic diameter of 571 μm. The evaporation rate is 0.01 $ml \cdot min^{-1}$.

For higher evaporation rates, perturbed interfaces are observed, as shown in Figure 14. This is followed by the onset of nucleation at the interface and then large scale vaporisation occurs. A frame rate of 1000 fps was used to capture nucleation as its incipience is rapid.

The meniscus of Al_2O_3-ethanol nanofluids was studied and compared to that of pure ethanol. A stable meniscus was observed with nanofluids at relatively low evaporation rates. Figure 15 compares the stable meniscus obtained with 0.01 vol.% Al_2O_3-ethanol nanofluid and pure ethanol at the same evaporation rate 0.03 ml·min^{-1}. The contact angles on the channel side-wall are θ_{nano} and θ_{pure} respectively. The nanofluid has a higher contact angle than pure ethanol. The meniscus in the channel was obtained by carefully ensuring all the experimental conditions are the same except for nanoparticles concentration. The added particles increase the suspension density, therefore the weight is larger. From a force balance, higher capillarity is expected. Therefore the surface tension must be higher with a larger contact angle (*i.e.* lower $\cos\theta$). Correspondingly the wettability was decreased.

Aside from the changed contact angle, the interface stability is also affected by the nanoparticles. At an evaporation rate of 0.04 ml·min^{-1} in a 571 μm micro-channel, the meniscus of pure ethanol is very unstable and is significantly deformed (Wang *et al*. [52]); however, the meniscus of a 0.01 vol.% nanofluid at the same evaporation rate is more stable. The interface oscillates slightly without being significantly deformed. This unstable meniscus for the nanofluid prevailed up to an evaporation rate of 0.07 ml·min^{-1} in the 571 μm micro-channel whereas the pure ethanol had undergone nucleation at a lower rate. This shows that nanoparticles substantially enhanced the meniscus stability even at a particle volume fraction of 0.01 vol.%.

Under heating conditions, the deposition and the building-up of a porous layer(s) of nanoparticles on the surface are likely (Vafaei and Wen [43]). In the present study, during evaporation this deposition of nanoparticles on the channel surface is observed and indeed results in increased local particle concentrations. Therefore, the local fluid viscosity is

increased. This increased viscosity, the pinning effect of the nanoparticles at the meniscus and the change of surface condition all help to stabilise the meniscus.

During the transition from a stable interface to a perturbed one, the nanofluid meniscus oscillated. The meniscus recedes with stick-slip drop and return to its original height. During evaporation, the reduction of ethanol left the nanoparticles on the channel inner surface. Closer inspection reveals that the nanoparticle deposition appears line by line following the receding meniscus. A similar "stick-slip" phenomenon was previously reported by Orejon *et al.* [52] and Moffat *et al*. [54]. They described the stick-slip pinning behaviour of the triple line during droplet evaporation and argued that the slip behaviour indicated the existence of hysteretic energy barriers and the stick behaviour was explained by locally increased viscosity or by the pinning of the deposited nanoparticles. The sudden return of meniscus to its original height occurred as the liquid pressure conquers the joint resistance from the surface tension force and the pinning of the nanoparticles.

Meniscus evaporation rate

The meniscus evaporation rate measurements are plotted against surface heat flux in Figure 16 for ethanol in various channels and the flux at which the large scale nucleation ensues is also indicated. The meniscus evaporation rate is an increasing function of heat flux. Evaporation rate is also affected by channel width when $q > 1.2$ kW·m^{-2}, showing an evaporation rate enhancement in larger micro-channels. This is expected because larger micro-channels have longer contact lines, where most of the evaporation takes place (Buffone and Sefiane [55, 56]). However, for $q < 1.2$ kW·m^{-2}, the evaporation rate is insensitive to the increasing heat flux. The heat can be considered to be stored in a superheated liquid layer near the interface before rapid evaporation occurs. Thus heat loss to the liquid is more profound at low heat flux conditions.

The evaporation rate per length of contact line, (the "specific evaporation rate") was also deduced. To estimate the contact line length, the inner perimeter, $2(W_{in} + d_{in})$, was used as electron microscopy revealed the radius of the corner to be negligibly small (101.84 micron). As shown in Figure 17, the curves of evaporation rate per length in the 571 μm and 762 μm channels almost overlap, showing that the evaporation rate in the rectangular micro-channel is proportional to the length of the contact line and is a function of the aspect ratio, σ. The specific evaporation rate is higher when the channel aspect ratio is lower.

Infrared measurements at and around the meniscus

Infrared measurements of the channel surface temperature profiles were recorded. Figure 18 (a) shows the IR image of the channel surface when a heat flux of 1.098 $kW \cdot m^{-2}$ for an evaporation rate of 0.01 $ml \cdot min^{-1}$ for which a stable interface without any deformation is observed. The evaporation is greatest at the meniscus contact line, lowering the local channel surface temperature.

The temperature reduction at the meniscus was seen in all the fluxes and evaporation rates studied. Selected IR images obtained in the 571 μm micro-channel are presented in Figs 19-21, with evaporation rates in the range 0.02 $ml \cdot min^{-1}$ to 0.06 $ml \cdot min^{-1}$ and including stable and unstable behaviour of the meniscus. For higher evaporation rates, a greater temperature gradient across the meniscus was observed. A lower vapour temperature is achieved while the liquid interface remains at the saturation temperature, therefore a higher temperature gradient is observed. The air and vapour mixture is then heated by the upper channel, and the vapour temperature increases from the meniscus.

From the temperature profiles across the channel surface around the meniscus region, it is seen that the temperature gradient varies along the meniscus, showing that the temperature

gradient is higher at the meniscus wedge than the middle of the meniscus. This agrees with Buffone and Sefiane [56]. The consequent uneven surface tension on the meniscus brings the hot liquid to the colder region and results in thermocapillary Marangoni convection. The temperature gradient along the meniscus is more obvious at higher evaporation rate. Some intense convection can be seen by high speed camera, but more precise measurements using Particle image velocimetry are needed to demonstrate Marangoni convection.

Data across the axial line which passes through the meniscus base (see Figure 22 where data are the acquired for 1454 μm channels) was extracted and averaged. Differences can be found between the stable and unstable interfaces. For stable interfaces, the temperature profiles along the centre line resemble shallow wide-mouthed valleys, whereas for unstable menisci the valleys are deeper and narrower. The temperature drop associated with this sink effect appears to increase with evaporation rate (Fig 22) and is greater for stable menisci. More experiments are needed to explore this meniscus sink effect further.

CONCLUSION

In this work, an extension to existing work on pressure drop and friction factor prediction is presented and this confirms the validity of correlations for friction factors in high aspect ratio microchannels with nanofluids.

The single phase fluid pressure drop did not vary very significantly with nanoparticle concentration. When flow boiling occurred, the two-phase flow pressure drop was unstable and fluctuating. The nanoparticle concentration affected the frequency and amplitude of these fluctuations. A sudden evaporation phenomenon is observed where the meniscus suddenly forms. From the heat transfer measurements it was found that heat transfer increased with the presence of nanoparticles compared with pure ethanol. The heat transfer coefficient during

boiling is greatly enhanced with the presence of nanoparticles. It appears to have a maximum at a nanoparticle concentration of 0.05% with about fivefold enhancement over pure ethanol. Future work would include the use of more intermediate concentrations of nanofluids especially in the vicinity of the observed peak at 0.05% in order to refine the optimum concentration estimate. Further experiments with microchannels of other aspect ratios will be performed to assess their effect.

From the two-phase visualisations, bubble confinement and deformation are reported; these are phenomena not usually seen in larger channels. The observations and measurements of the two-phase flows were performed for the same conditions as those for the single evaporating meniscus and this fundamental approach should lead to a better understanding of contact line dynamics in two-phase flows. The study of heat and mass transfer near the three phase contact line reveals the important role played by this zone in two phase flow boiling in microchannels.

NOMENCLATURE

A area

C_p specific heat capacity

d diameter

f friction factor

G mass flux

h convective heat transfer coefficient

K loss coefficient

l length

m mass flowrate

P pressure

q heat flux

Re Reynolds number

T temperature

u velocity

W width

z distance along channel

Greek Symbols

θ angleμ viscosity

ρ density

σ aspect ratio

ϕ volume fraction

REFERENCES

[1] Lin, S., Sefiane, K., and Christy, J.R.E., Prospects of confined flow boiling in thermal management of microsystems, *Applied Thermal Engineering* , Vol. 22 no. 7, pp. 825-837, 2002.

[2] Barber, J., Brutin, D., Sefiane, Gardarein, J.L., and Tadrist, L., Unsteady-state fluctuations analysis during bubble growth in a "rectangular" microchannel , *International Journal of Heat and Mass Transfer* Vol. 54 no. 23-24, pp. 4784-4795, 2011.

[3] Barber, J., Brutin, D., Sefiane, K., and Tadrist, L., Bubble confinement in flow boiling of FC-72 in a "rectangular" microchannel of high aspect ratio , *Experimental Thermal and Fluid Science*, Vol.34 no. 8, pp.1375-1388, 2010.

[4] Barber, J., Sefiane, K., D. Brutin, D., and Tadrist, L., Hydrodynamics and heat transfer during flow boiling instabilities in a single microchannel. *Applied Thermal Engineering,* Vol. 29 no. 7, pp. 1299-1308, 2009.

[5] Bogojevic, D., K. Sefiane, K., Walton, A.J., H. Lin,H., and Cummins, G., Two-phase flow instabilities in a silicon microchannels heat sink. *International Journal of Heat and Fluid Flow*, Vol. 30 no. 5, pp. 854-867, 2009.

[6] Bogojevic, D., Sefiane, K., Walton, A.J., H. Lin, H., Cummins, G., Kenning, D.B.R., and Karayiannis, T.G., Experimental investigation of non-uniform heating effect on flow boiling instabilities in a microchannel-based heat sink, *International Journal of Thermal Sciences,* Vol 50 no. 3, pp. 309-324, 2011.

[7]S.U.S. Choi, S.U.S., and Eastman, J.A., Enhancing thermal conductivity of fluids with nanoparticles. International mechanical engineering congress and exhibition, San Francisco, CA (United States) p. 8, 1995.

[8] Xuan, Y. and W. Roetzel, W., Conceptions for heat transfer correlation of nanofluids. *International Journal of Heat and Mass Transfer*, Vol. 43 no. 19, pp. 3701-3707, 2000.

[9] Xie, H. Wang, J., Xi, T., Liu Y., and Ai, F., Dependence of the thermal conductivity of nanoparticle-fluid mixture on the base fluid. *Journal of Materials Science Letters*, Vol. 21 no. 19, pp. 1469-1471, 2002.

[10] Kumar Das, S., Putra, N., Thiesen P., and Roetzel, W., Temperature Dependence of Thermal Conductivity Enhancement for Nanofluids. *Journal of Heat Transfer*, Vol. 125 no. 4, pp. 567-574, 2003.

[11] Hwang, Y.J., Ahn, Y.C., Shin, H.S., Lee, C.G., Kim, G.T., Park, H.S., and Lee, J.K., Investigation on characteristics of thermal conductivity enhancement of nanofluids. *Current Applied Physics*, Vol. 6 no. 6, pp. 1068-1071, 2006.

[12] Lee, J.-H., Hwang, K.S., Jang, S.P., Lee, B.H., Kim, J.H., Choi S.U.S.,and Choi, C.J., Effective viscosities and thermal conductivities of aqueous nanofluids containing low volume concentrations of Al_2O_3 nanoparticles. *International Journal of Heat and Mass Transfer*, Vol. 51 no. 11-12, pp. 2651-2656, 2008.

[13] Li, X.F. . Zhu, D.S., Wang, X.J., Wang, N., Gao J.W., and. Li, H., Thermal conductivity enhancement dependent pH and chemical surfactant for Cu-H2O nanofluids. *Thermochimica Acta*, Vol. 469 no. 1-2, pp. 98-103, 2008.

[14] Murshed,S.M.S., Leong, K.C., and Yang, C., Investigations of thermal conductivity and viscosity of nanofluids. *International Journal of Thermal Sciences*, Vol. 47 no. 5, pp. 560-568, 2008.

[15] Wensel, J., Wright, B., Thomas, D., Douglas, W., Mannhalter, B., Cross, W., Hong, H.,. Kellar, J., Smith P., and Roy, W., Enhanced thermal conductivity by aggregation in heat transfer nanofluids containing metal oxide nanoparticles and carbon nanotubes. *Applied Physics Letters*, Vol. 92 no. 2, pp. 023110-023110-3, 2008.

[16] Xuan, Y., and Li, Q., Heat transfer enhancement of nanofluids. *International Journal of Heat and Fluid Flow*, Vol. 21 no. 1, pp. 58-64, 2000.

[17] Hong, T.-K., Yang, H.-S., and Choi, C.J., Study of the enhanced thermal conductivity of Fe nanofluids. *Journal of Applied Physics*, Vol. 97 no. 6, pp.064311-064311-4, 2005.

[18] Hwang, K.S., Jang S.P., and Choi, S.U.S., Flow and convective heat transfer characteristics of water-based Al_2O_3 nanofluids in fully developed laminar flow regime. *International Journal of Heat and Mass Transfer*, Vol. 52 no. 1-2, pp. 193-199, 2009.

[19]U. Rea, T. McKrell, L.-W. Hu and J. Buongiorno, Laminar convective heat transfer and viscous pressure loss of alumina-water and zirconia-water nanofluids. *International Journal of Heat and Mass Transfer*, Vol. 52 no. 7-8, pp. 2042-2048, 2009.

[20] Duangthongsuk, W., and Wongwises, S., An experimental study on the heat transfer performance and pressure drop of TiO2-water nanofluids flowing under a turbulent flow regime. *International Journal of Heat and Mass Transfer*, Vol. 53 no. 1-3, pp. 334-344, 2010.

[21] Williams, W., Buongiorno, J., and Hu, L.-W., Experimental Investigation of Turbulent Convective Heat Transfer and Pressure Loss of Alumina/Water and Zirconia/Water Nanoparticle Colloids (Nanofluids) in Horizontal Tubes. *Journal of Heat Transfer*, Vol. 130 no. 4, pp. 042412, 2008.

[22] Chopkar, M., Das, A., Manna, I., and Das, P., Pool boiling heat transfer characteristics of ZrO2–water nanofluids from a flat surface in a pool. *Heat and Mass Transfer*, Vol. 44 no. 8, pp. 999-1004, 2008.

[23] Trisaksri, V., and Wongwises, S., Nucleate pool boiling heat transfer of TiO2-R141b nanofluids. *International Journal of Heat and Mass Transfer*, Vol. 52 no. 5-6, pp. 1582-1588, 2009.

[24] Park, K.-J., and Jung, D., Enhancement of nucleate boiling heat transfer using carbon nanotubes. *International Journal of Heat and Mass Transfer*, Vol. 50 no. 21-22, pp. 4499-4502, 2007.

[25] Park, K.-J., and Jung, D., Boiling heat transfer enhancement with carbon nanotubes for refrigerants used in building air-conditioning. *Energy and Buildings*, Vol. 39 no. 9, pp. 1061-1064, 2007.

[26] Li, Y., Zhou, J.E., Tung, S., Schneider E., and Xi, S., A review on development of nanofluid preparation and characterization. *Powder Technology*, Vol. 196 no. 2, pp. 89-101, 2009.

[27] Sharma, K.V., Sundar L.S., and Sarma, P.K., Estimation of heat transfer coefficient and friction factor in the transition flow with low volume concentration of Al_2O_3 nanofluid flowing in a circular tube and with twisted tape insert. *International Communications in Heat and Mass Transfer*, Vol. 36 no. 5, pp. 503-507, 2009.

[28] Dong, L., and Leyuan, Y., Single-Phase Thermal Transport of Nanofluids in a Minichannel. *Journal of Heat Transfer*, Vol.133 no. 3, pp. 031009, 2011.

[29] Xuan, Y., and Li, Q., Investigation on Convective Heat Transfer and Flow Features of Nanofluids. *Journal of Heat Transfer*, Vol. 125 no. 1, pp. 151-155, 2003.

[30] Fotukian, S.M., and Nasr Esfahany, M., Experimental study of turbulent convective heat transfer and pressure drop of dilute CuO/water nanofluid inside a circular tube. *International Communications in Heat and Mass Transfer*, Vol. 37 no. 2, pp. 214-219, 2010.

[31] Li, Q., and Xuan, Y., Convective heat transfer and flow characteristics of Cu-water nanofluid. *Science in China Series E: Technological Sciences*, Vol. 45 no. 4, pp. 408-416, 2002.

[32]. Das, S.K., N. Putra, N., and W. Roetzel, W., Pool boiling characteristics of nano-fluids, *International Journal of Heat and Mass Transfer*, Vol. 46, pp. 851-862, 2003.

[33] Wen, D., Ding, Y., Experimental investigation into the pool boiling heat transfer of aqueous based γ-alumina nanofluids, *Journal of Nanoparticle Research*, Vol. 7, pp. 265-274, 2005.

[34] White, S.B., Enhancement of Boiling Surfaces using Nanofluid particle deposition, Ph.D. thesis, University of Michigan, 2010.

[35] Zeinali Heris, S., Experimental investigation of pool boiling characteristics of low-concentrated CuO/ethylene glycol–water nanofluids, *International Communications in Heat and Mass Transfer*, Vol. 38, pp. 1470-1473, 2011.

[36] Kole, M., and Dey, T.K., Investigations on the pool boiling heat transfer and critical heat flux of ZnO-ethylene glycol nanofluids, *Applied Thermal Engineering*, Vol 37, pp. 112-119, 2012.

[37] Chang, T.-B., Syu, S.-C., and Yang, Y.-K., Effects of particle volume fraction on spray heat transfer performance of Al_2O_3–water nanofluid, *International Journal of Heat and Mass Transfer*, Vol. 55, pp. 1014-1021, 2012.

[38] Liu, Z.-H., Xiong, J.-G., and Bao, R., Boiling heat transfer characteristics of nanofluids in a flat heat pipe evaporator with micro-grooved heating surface, *International Journal of Multiphase Flow*, Vol. 33, pp. 1284-1295, 2007.

[39] Yang, X.F., Liu, Z.-H., and Zhao, J., Heat transfer performance of a horizontal micro-grooved heat pipe using CuO nanofluid, *Journal of Micromechanics and Microengineering*, Vol. 18, p. 6., 2008.

[40] Jung, J.-Y., Kim, E.S., and Kang, Y.T., Stabilizer effect on CHF and boiling heat transfer coefficient of alumina/water nanofluids, *International Journal of Heat and Mass Transfer*, Vol. 55, pp. 1941-1946, 2012.

[41] Huminic, G., and Huminic, A., Heat transfer characteristics of a two-phase closed thermosyphons using nanofluids, *Experimental Thermal and Fluid Science*, Vol. 35, pp. 550-557, 2011.

[42] Wen, D., Influence of nanoparticles on boiling heat transfer, *Applied Thermal Engineering*, Vol. 41, pp. 2-9, 2012.

[43] Vafaei, S., and Wen, D., Critical Heat Flux (CHF) of Subcooled Flow Boiling of Alumina Nanofluids in a Horizontal Microchannel, *Journal of Heat Transfer*, Vol. 132, pp. 102404-102407, 2010.

[44] Kim, T.I., Jeong, Y.H., and Chang, S.H., An experimental study on CHF enhancement in flow boiling using Al_2O_3 nano-fluid, *International Journal of Heat and Mass Transfer*, Vol. 53 pp. 1015-1022, 2010.

[45] Henderson, K., Park, Y.-G., Liu, L., and Jacobi, A.M., Flow-boiling heat transfer of R-134a-based nanofluids in a horizontal tube, *International Journal of Heat and Mass Transfer*, Vol. 53, pp. 944-951, 2010.

[46] Park, Y., Liu, L., and Sommers, A., Two-phase flow-boiling of refrigerant-based nanofluid in a horizontal tube, *International conference on cryogenics and refrigeration. Cryognenics and refrigeration proceedings*, Hangzhou, China, pp. 954-963, 2008.

[47] Mohammed, H.A., Bhaskaran, G., Shuaib, N.H., and Abu-Mulaweh, H.I., Influence of nanofluids on parallel flow square microchannel heat exchanger performance, *International Communications in Heat and Mass Transfer*, Vol. 38, pp. 1-9, 2011.

[48] White, F.M., *Fluid Mechanics*. McGraw-Hill,New York, 1986.

[49] Shah, R.K., and London, A.L., *Laminar flow forced convection in ducts: a source book for compact heat exchanger analytical data*. Academic Press. New York, 1978.

[50] Shah, R.K., and London, A.L., *Laminar flow forced convection in ducts : a source book for compact heat exchanger analytical data*. New York,. Academic Press, 1978.

[51] Brinkman, H.C., The Viscosity of Concentrated Suspensions and Solutions. *The Journal of Chemical Physics*, Vol. 20 no. 4, p. 571, 1952.

[52] Wang, Y., Sefiane, K., and Wang, Z., Evaporating Meniscus of Ethanol and Ethanol-based Nanofluids in Single Micro-Channels, *Applied Mechanics and Materials* Vol. 39, pp. 685-690, 2013.

[53] Orejon, D., Sefiane, K., and Shanahan, M.E., Stick-slip of evaporating droplets: substrate hydrophobicity and nanoparticle concentration, *Langmuir*, Vol. 27 no. 21, pp. 12834-43, 2011.

[54] Moffat, J.R., Sefiane, K., and Shanahan, M.E.R., Effect of TiO_2 Nanoparticles on Contact Line Stick−Slip Behavior of Volatile Drops. *The Journal of Physical Chemistry B*, Vol. 113 no. 26, pp. 8860-8866, 2009.

[55] Buffone, C., and Sefiane, K., IR measurements of interfacial temperature during phase change in a confined environment. *Experimental Thermal and Fluid Science*, Vol.29 no. 1, pp. 65-74, 2004.

[56] Buffone, C., and Sefiane, K., Temperature measurement near the triple line during phase change using thermochromic liquid crystal thermography. *Experiments in Fluids*, Vol. 39 no. 1, pp. 99-110, 2005.

Captions

Figure 1. Experimental setup (a) transparent heated channel, (b) schematic of high-aspect ratio channel.

Figure 2. Ethanol-based Al_2O_3 nanofluids, 0.01 vol%, made by ultrasonic bath.

Figure 3. Micro-channel test section and connecting pipes showing the locations of expansion and contraction.

Figure 4. Comparisons of the measured friction factors with conventional friction correlation (a) d_h = 571 μm, (b) d_h = 762 μm, (c) d_h = 1454 μm; ethanol-based Al_2O_3 nanofluids.

Figure 5. Pressure drop measurements, d_h = 1454 μm, G = 11.2 kg·m^{-2}·s^{-1}, (a) single phase flow without heating, (b) two-phase flow at q = 7.0 kW·m^{-2}; ethanol.

Figure 6. Inlet and outlet pressures, d_h = 571 μm, G = 44.8 kg·m^{-2}·s^{-1}, q = 6.90 kW·m^{-2}.

Figure 7. Example of transient channel wall temperature profile from the infrared camera.

Figure 8. Heat transfer coefficient distribution along the channel, at various nanofluid concentrations (a) Power= 1.5 kW/m^2 and (b) Power= 9kW/m^2

Figure 9. Heat transfer coefficient for pure ethanol and three concentrations of Al_2O_3-ethanol nanofluid at different points of the channel test section – (a) Re = 4.5 and q_{input} = 4.5 kW·m^{-2} , (b) Re = 11.3 and q_{input} =7.5 kW·m^{-2} and (c) Re = 18.1 and q_{input} =7.5 kW·m^{-2}

Figure 10 . A sequence of bubble growth, confinement and two phase flow boiling within transparent-heated microchannel.

Figure 11. Flow patterns for boiling in a microchannel

Figure 12. Schematic drawing of the forces at the meniscus in a vertical micro-channel

Figure 13. Deformed interface in the channel with d_h = 571 μm at evaporation rate 0.05 ml·min^{-1}, ethanol, camera speed: 200 fps. The "L" and "v" in the figures represent the liquid and the air-vapour sides respectively.

Figure 14. Nucleation at interface in the channel with d_h = 571 μm at evaporation rate 0.05 ml·min^{-1}, ethanol, camera speed: 1000 fps

Figure 15. Contact angle comparison in the channel with d_h = 571 μm, evaporation rate 0.03 ml·min^{-1} between (a) Al_2O_3-ethanol nanofluids, 0.01 vol.% and (b) pure ethanol; camera speed, 200 fps.

Figure 16. Meniscus evaporation rate versus heat flux in three micro-channels; pure ethanol.

Figure 17. Evaporation rate per unit length versus heat flux

Figure 18. (a) IR image of the temperature profile in the channel with d_h = 571 μm at evaporation rate of 0.01 ml·min^{-1} and q = 1.098 kW·m^{-2}, stable interface, ethanol, (b) 3-dimensional plot

Figure 19. (a) IR image of the temperature profile in the channel with d_h = 571 μm at evaporation rate of 0.02 ml·min^{-1} and q = 1.357 kW·m^{-2}, stable interface, ethanol, (b) 3-dimensional plot

Figure 20. (a) IR image of the temperature profile in the channel with d_h = 571 μm at evaporation rate of 0.05 ml·min^{-1} and q = 2.969 kW·m^{-2}, unstable interface, ethanol, (b) 3-dimensional plot.

Figure 21. (a) IR image of the temperature profile in the channel with d_h = 571 μm at evaporation rate of 0.06 ml·min^{-1} and q = 3.318 kW·m^{-2}, unstable interface, ethanol, (b) 3-dimensional plot.

Figure 22. Temperature profiles along the channel central line in the channel with d_h = 1454 μm; ethanol

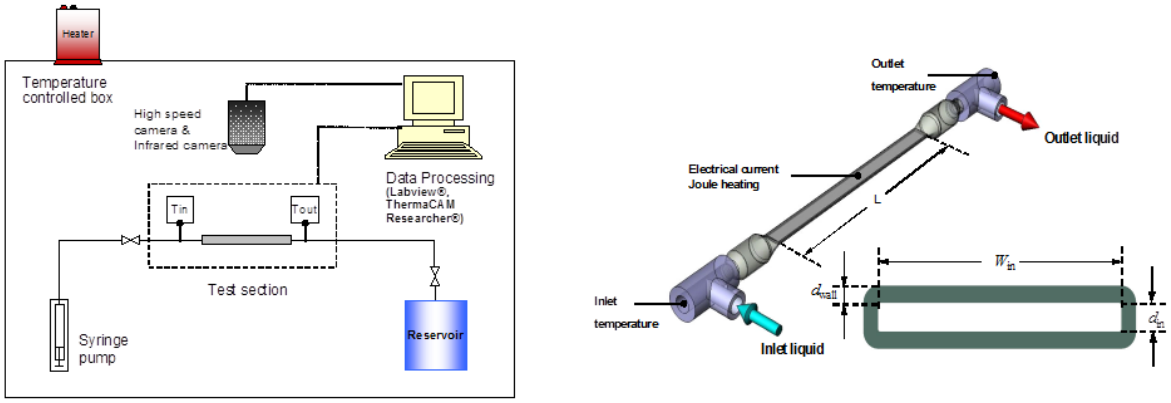
Heater
Temperature controlled box
High speed camera & Infrared camera
Data Processing (Labview®, ThermaCAM Researcher®)
Tin
Tout
Test section
Syringe pump
Reservoir
Outlet temperature
Outlet liquid
Electrical current Joule heating
L
Inlet temperature
Inlet liquid

Fig. 1

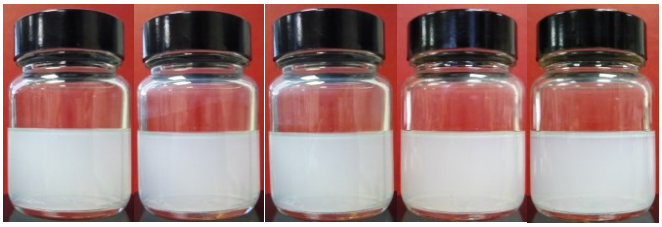

Fig. 2

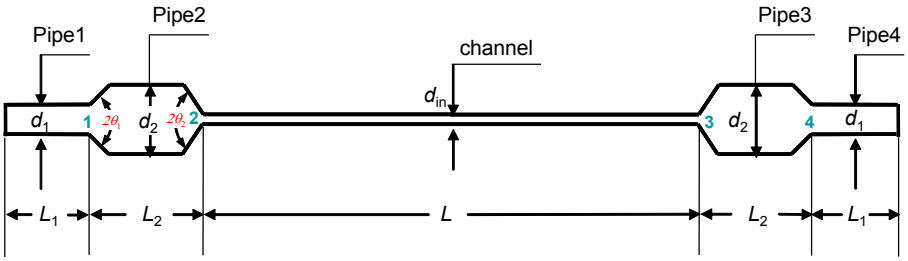
Pipe1
Pipe2
channel
Pipe3
Pipe4
d_{in}
d_1
1
$2\theta_1$
d_2
$2\theta_2$
2
3
d_2
4
d_1
L_1
L_2
L
L_2
L_1

Fig. 3

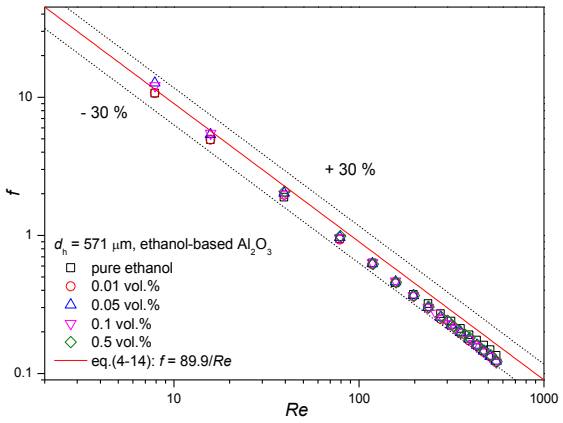

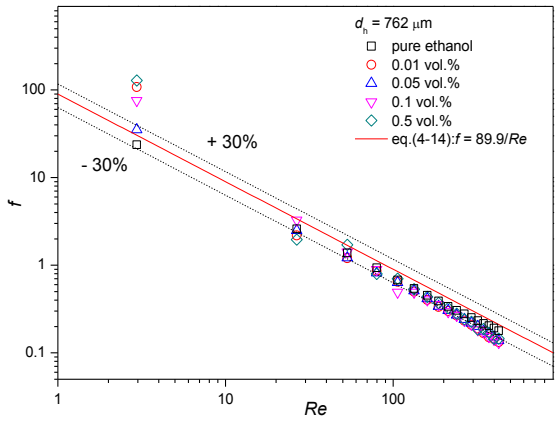

(a) **(b)**

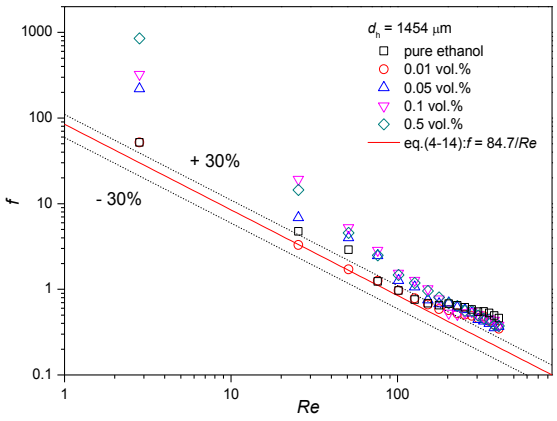

(c)Fig. 4

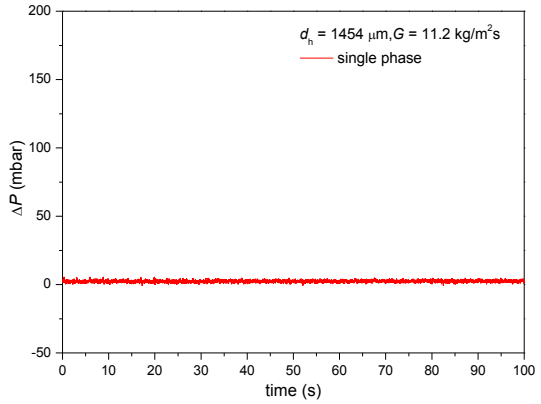

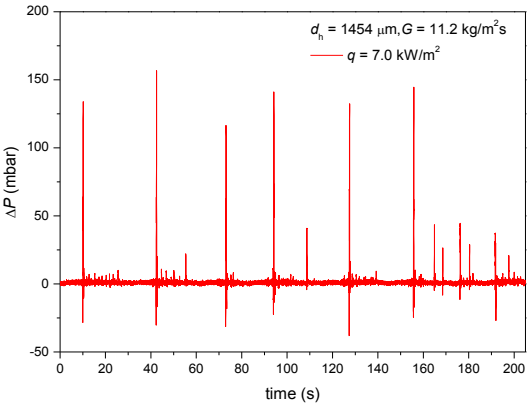

(a) (b)

Fig. 5

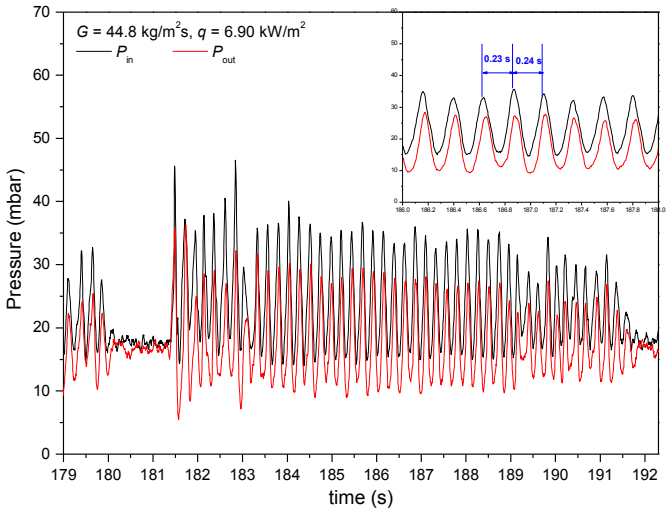
G = 44.8 kg/m²s, q = 6.90 kW/m²
P in
P out
0.23 s
0.24 s
Pressure (mbar)
time (s)
0
10
20
30
40
50
60
70
179
180
181
182
183
184
185
186
187
188
189
190
191
192

Fig. 6

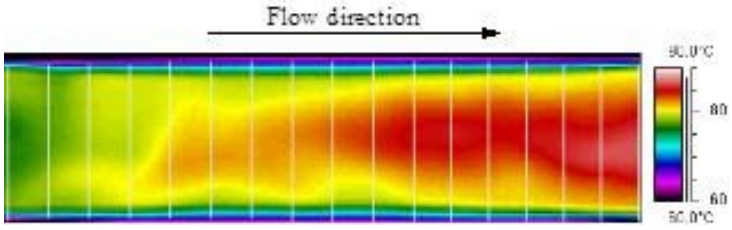

Fig. 7

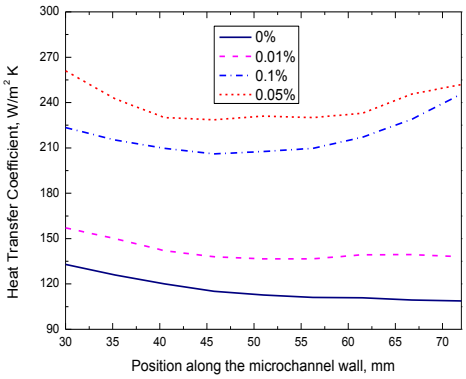
Heat Transfer Coefficient, W/m^2 K
Position along the microchannel wall, mm
0%
0.01%
0.1%
0.05%

(a)

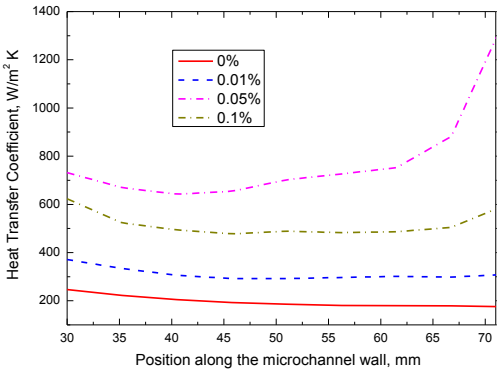
Heat Transfer Coefficient, W/m^2 K
Position along the microchannel wall, mm
0%
0.01%
0.05%
0.1%

(b)

Fig. 8

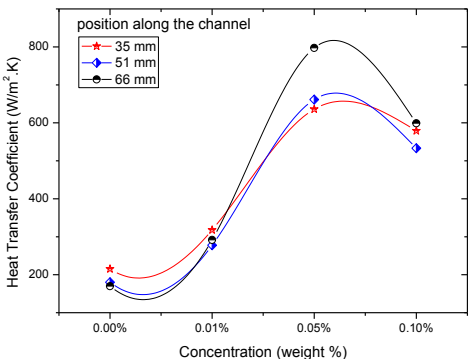
position along the channel
35 mm
51 mm
66 mm
Heat Transfer Coefficient (W/m².K)
800
600
400
200
0.00%
0.01%
0.05%
0.10%
Concentration (weight %)

(a)

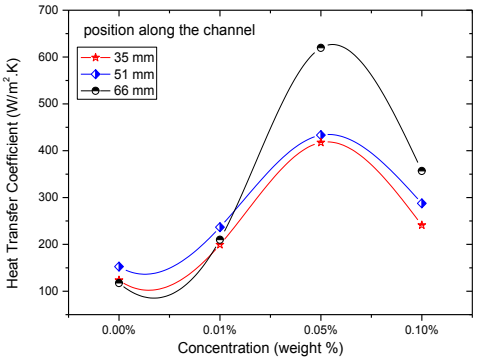
position along the channel
35 mm
51 mm
66 mm
Heat Transfer Coefficient (W/m².K)
700
600
500
400
300
200
100
0.00%
0.01%
0.05%
0.10%
Concentration (weight %)

(b)

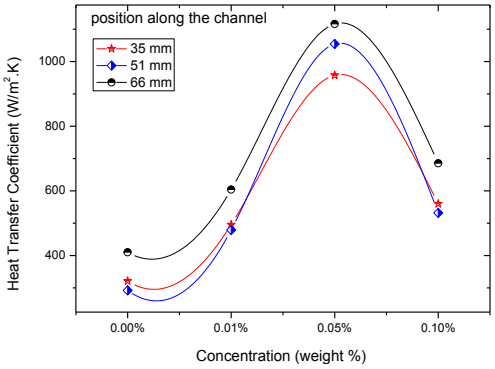
position along the channel
35 mm
51 mm
66 mm
Heat Transfer Coefficient (W/m².K)
1000
800
600
400
0.00%
0.01%
0.05%
0.10%
Concentration (weight %)

(c)

Fig. 9

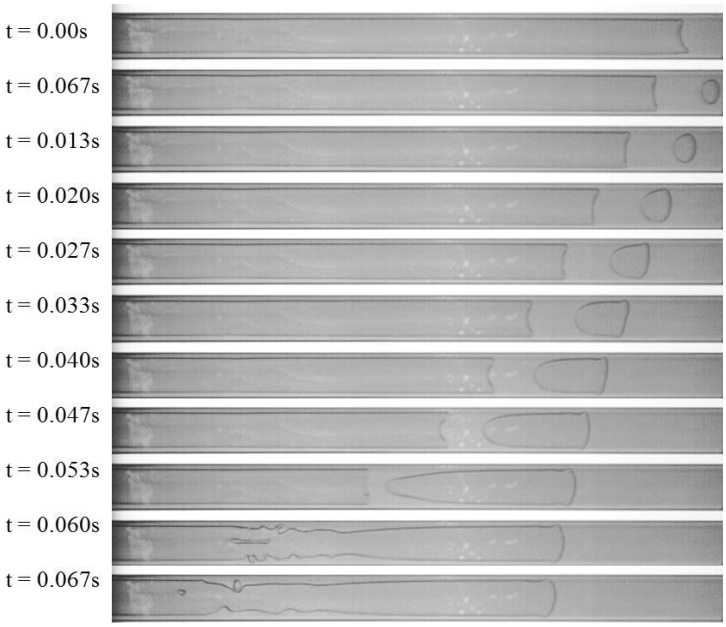
t = 0.00s
t = 0.067s
t = 0.013s
t = 0.020s
t = 0.027s
t = 0.033s
t = 0.040s
t = 0.047s
t = 0.053s
t = 0.060s
t = 0.067s

Fig. 10

Slug flow

Annular flow

Liquid ring flow

Meniscus

Fig. 11

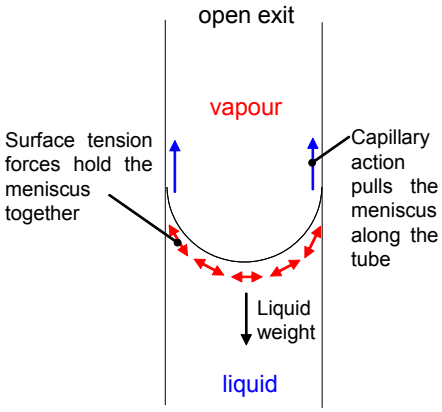
open exit
vapour
Surface tension forces hold the meniscus together
Capillary action pulls the meniscus along the tube
Liquid weight
liquid

Fig. 12

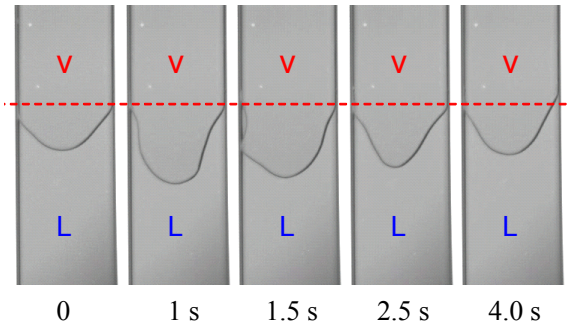

Fig. 13

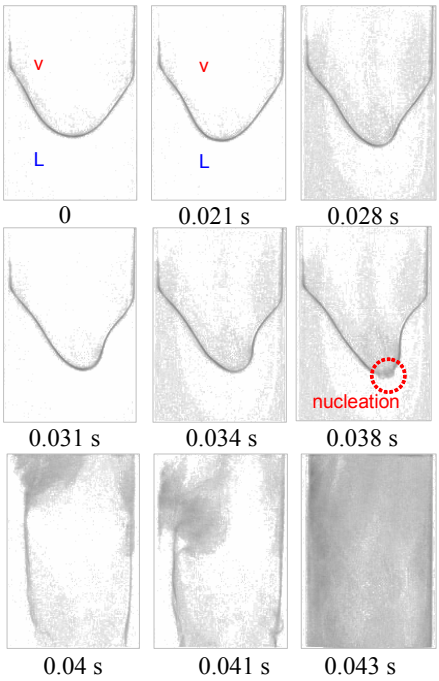
v
L
0
v
L
0.021 s
0.028 s
0.031 s
0.034 s
nucleation
0.038 s
0.04 s
0.041 s
0.043 s

Fig. 14

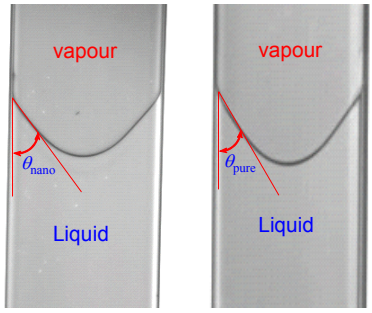

(a) **(b)**

Fig. 15

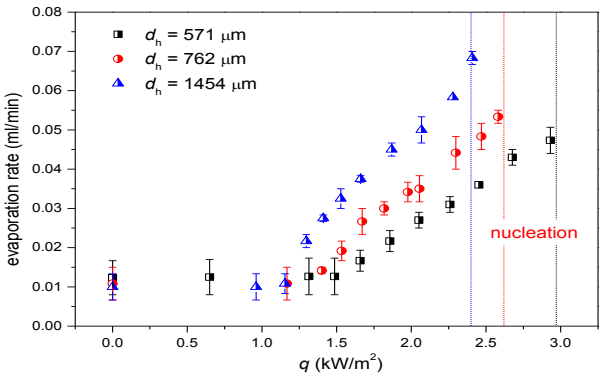
d_h = 571 μm
d_h = 762 μm
d_h = 1454 μm
nucleation
evaporation rate (ml/min)
q (kW/m^2)
0.00
0.01
0.02
0.03
0.04
0.05
0.06
0.07
0.08
0.0
0.5
1.0
1.5
2.0
2.5
3.0

Fig. 16

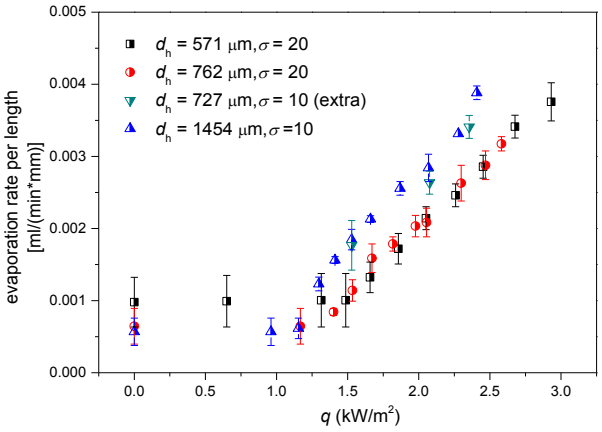
0.005
0.004
0.003
0.002
0.001
0.000
0.0
0.5
1.0
1.5
2.0
2.5
3.0
evaporation rate per length
[ml/(min*mm)]
q (kW/m2)
dh = 571 μm,σ = 20
dh = 762 μm,σ = 20
dh = 727 μm,σ = 10 (extra)
dh = 1454 μm,σ =10

Fig. 17

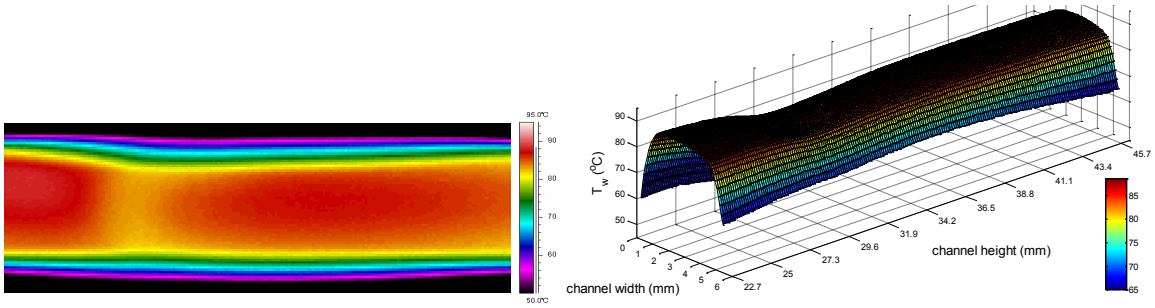
95.0°C
90
80
70
60
50.0°C
T_w (°C)
90
80
70
60
50
0
1
2
3
4
5
6
channel width (mm)
22.7
25
27.3
29.6
31.9
34.2
36.5
38.8
41.1
43.4
45.7
channel height (mm)
85
80
75
70
65

(a) **(b)**

Fig. 18

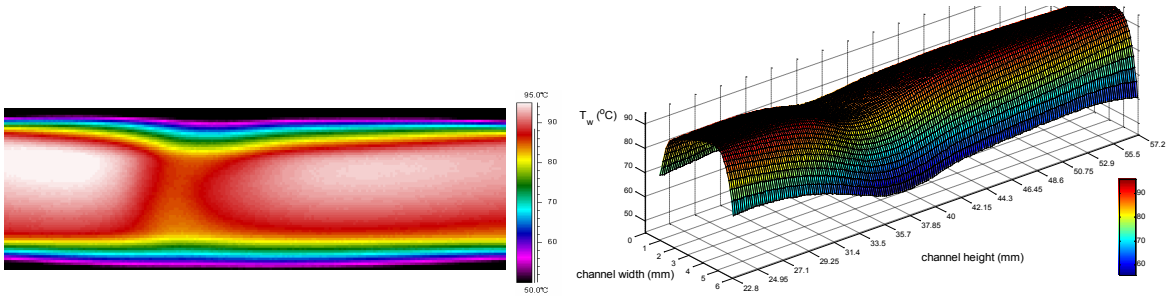
95.0℃
90
80
70
60
50.0℃
T_w (°C)
90
80
70
60
50
0
1
2
3
4
5
6
channel width (mm)
22.8
24.95
27.1
29.25
31.4
33.5
35.7
37.85
40
42.15
44.3
46.45
48.6
50.75
52.9
55.5
57.2
channel height (mm)

(a) **(b)**

Fig. 19

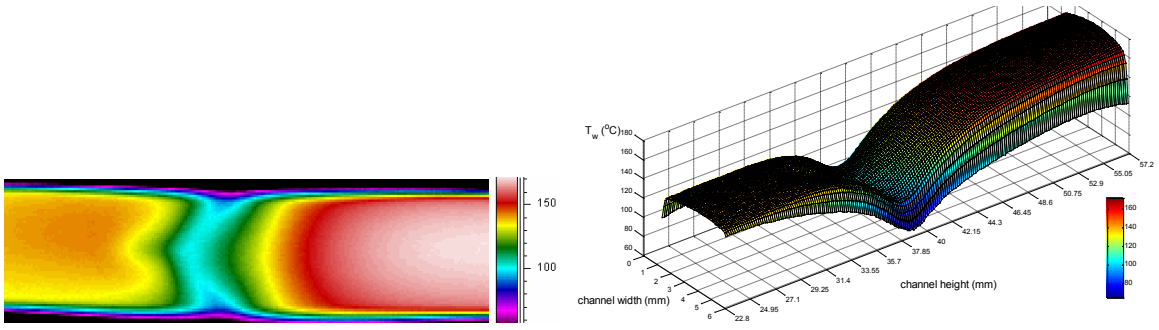

(a) **(b)**

Fig. 20

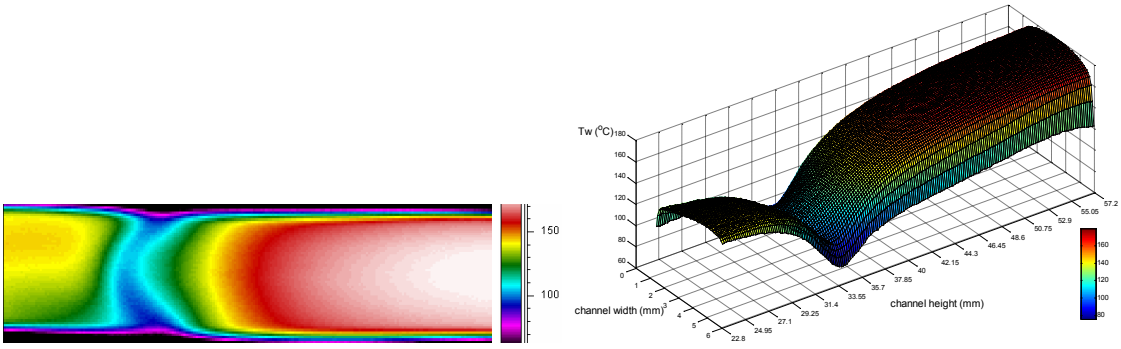
150
100
Tw (°C)
180
160
140
120
100
80
60
0
1
2
3
4
5
6
channel width (mm)
22.8
24.95
27.1
29.25
31.4
33.55
35.7
37.85
40
42.15
44.3
46.45
48.6
50.75
52.9
55.05
57.2
channel height (mm)
160
140
120
100
80

(a) **(b)**

Fig. 21

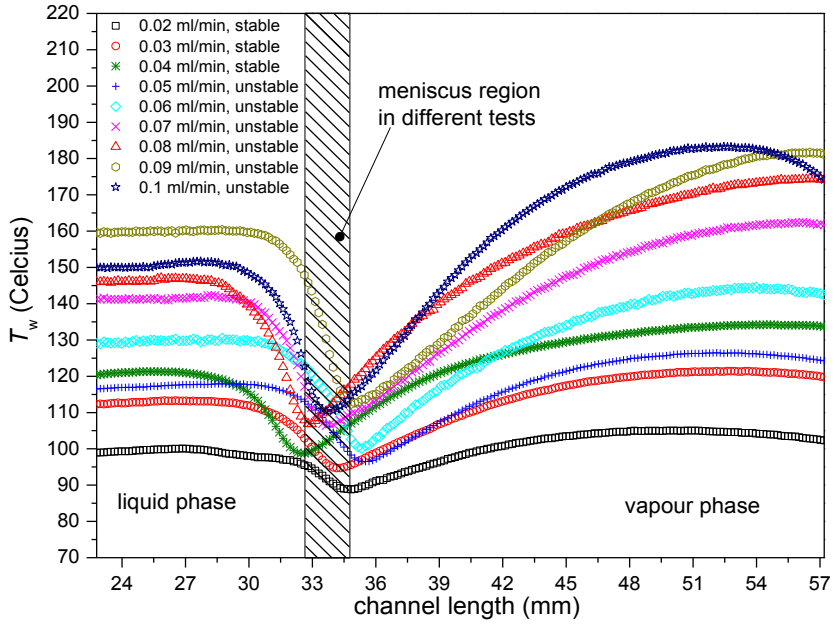
0.02 ml/min, stable
0.03 ml/min, stable
0.04 ml/min, stable
0.05 ml/min, unstable
0.06 ml/min, unstable
0.07 ml/min, unstable
0.08 ml/min, unstable
0.09 ml/min, unstable
0.1 ml/min, unstable
meniscus region
in different tests
liquid phase
vapour phase
T_w (Celcius)
channel length (mm)
220
210
200
190
180
170
160
150
140
130
120
110
100
90
80
70
24
27
30
33
36
39
42
45
48
51
54
57

Fig. 22

Biographical details

Gail Duursma obtained her first degree in Chemical Engineering from University of Cape Town and her D.Phil from University of Oxford and is currently a Lecturer in Chemical Engineering at the University of Edinburgh.

Khellil Sefiane has MSc and PhD degrees in Chemical Engineering. He is presently Professor and ExxonMobil Fellow at the University of Edinburgh and is Head of the Institute of Materials and Processes.

Alexandre Dehaene was a student at ENSIAME, Université de Valenciennes, who did a placement at the University of Edinburgh.

Souad Harmand is a Professor of Engineering at ENSIAME, Université de Valenciennes, France. She is vice-president of the Université de Valenciennes and leader of the research team TEMPO.

Yuan Wang obtained her PhD from the University of Edinburgh and now works at the Science and Technology on Scramjet Laboratory of the National University of Defense Technology, in Hunan, China.